**Table 3.10:** The atomic coordinates from the DFT geometry optimisation of $Li(NH_3)_4BH_4$.

| atom | site | x | y | z |
|---|---|---|---|---|
| H | H1 | 0.33800 | 0.39244 | 0.24412 |
| H | H2 | 0.73897 | 0.13279 | 0.58330 |
| H | H3 | 0.09644 | 0.36573 | 0.53609 |
| H | H4 | 0.98507 | 0.56337 | 0.82651 |
| H | H5 | 0.84888 | 0.57050 | 0.79031 |
| H | H6 | 0.89490 | 0.43796 | 0.91666 |
| N | N7 | 0.91317 | 0.48255 | 0.82060 |
| H | H8 | 0.38751 | 0.25000 | 0.40876 |
| H | H9 | 0.22558 | 0.25000 | 0.35628 |
| H | H10 | 0.80196 | 0.25000 | 0.46054 |
| H | H11 | 0.13997 | 0.25000 | 0.66860 |
| Li | Li1 | 0.92562 | 0.25000 | 0.69431 |
| B | B1 | 0.32193 | 0.25000 | 0.31279 |
| N | N1 | 0.78750 | 0.25000 | 0.56279 |
| N | N2 | 0.07918 | 0.25000 | 0.59529 |

Clear images of the structure are shown in Figures 3.33 and 3.37, where it can be seen that $Li(NH_3)_4^+$ tetrahedra run in rows in the y-direction, and these are connected to neighbouring rows via the $BH_4^-$ anion. Neighbouring rows form layers that span the the yz-plane, the layers are made up of either $Li(NH_3)_4^+$ or $BH_4^-$ and dihydrogen bonding is observed between alternate layers as highlighted in Figure 3.26. These layers are also seen in $Li(NH_3)_4Br$ and $Li(NH_3)_4I$, however in $Li(NH_3)_4BH_4$ they are more clearly defined.

Both $Li(NH_3)_4Br$ (and $Li(NH_3)_4I$) have previously been described as having a distorted CsCl structure,[103] similar to that shown in Figure 3.27. This is because each Li atom is coordinated by 8 Br atoms at Li−Br distances of; 4.75, 4.58, 4.73, 4.73, 5.43, 5.48, 5.43, and 7.54 Å (with similar distances seen in the Iodide). The comparison with CsCl is attractive, but the single longer bond length raises concern. In $Li(NH_3)_4BH_4$, the equivalent Li−B distances are; 4.72, 4.81, 4.92, 4.81, 4.91, 4.92, 6.11, and 7.84 Å. In this case the two long bond-lengths are towards the atoms on

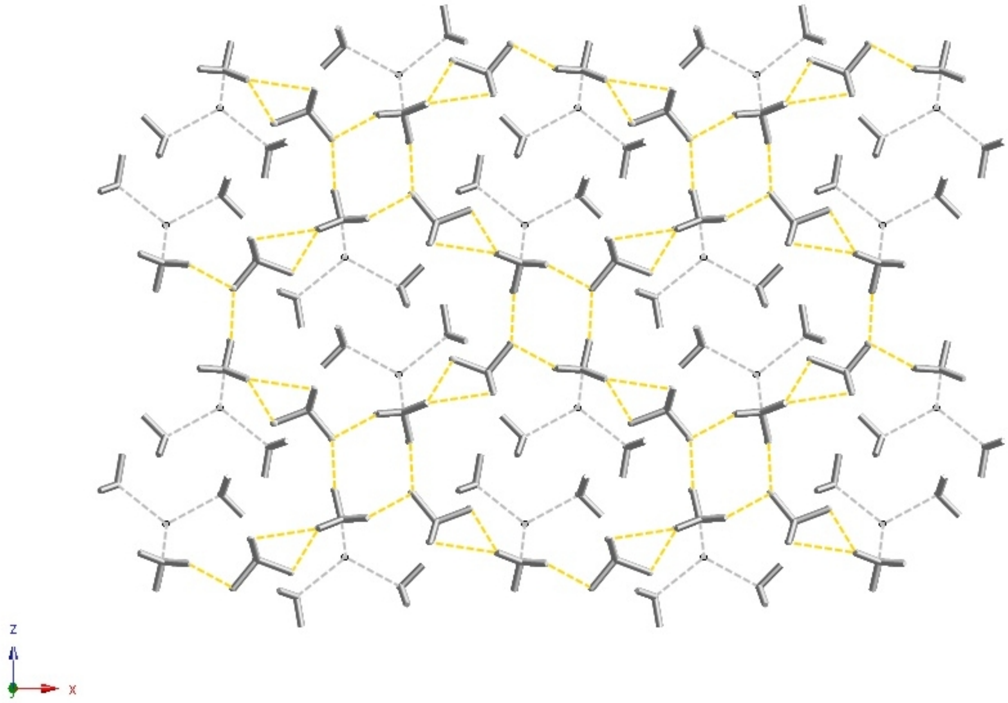

**Figure 3.26:** The structure of Li$(NH_3)_4BH_4$, highlighting dihydrogen bonding. Li−B bonds are shown as dashed grey lines and NH···HB contacts of ≤ 95 % of the Van der Waals radii (i.e. 2.28 Å) as dashed gold lines

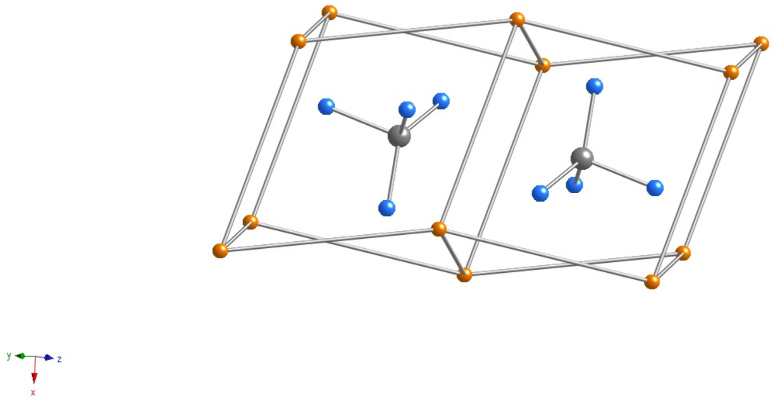

**Figure 3.27:** Li$(NH_3)_4BH_4$ showing the distorted CsCl motif as observed in the Rietveld refined structure and originally proposed by Jacobs et al. for Li$(NH_3)_4$Br and Li$(NH_3)_4$I. H atoms are omitted for clarity, Li in grey, B in brown and N in blue.

opposite corners of the distorted CsCl cell. When considering just the 6 nearest neighbours it is apparent that the Li atoms sit inside distorted $LiB_6$ octahedra. At this point the experimental and calculated structures differ significantly; in the experimental structure the $LiB_6$ octahedra are arranged in face sharing chains that are vertex linked to neighbouring chains, in the calculated structure these chains are edge-sharing, as shown in Figure 3.28. The environment of the B atoms is more striking; in the experimental structure the B atoms sit inside edge sharing but distorted $BLi_6$ trigonal prisms, while in the calculated structure the arrangement is of edge-sharing $BLi_6$ octahedra, as shown in Figure 3.29. These structure types are well known, albeit somewhat distorted, as NiAs and NaCl for the experimental and calculated structures respectively. Typically the NiAs structure is observed where metal-metal bonding is favourable; in this case it is proposed that the proximity of $Li(NH_3)_4^+$ cations allows for increased $NH_3$ mobility, thus promoting the observed disorder. This ammonia mobility has not been modelled in the DFT calculations, and therefore the energy is lowered as the $Li(NH_3)_4^+$ tetrahedra move apart and NaCl type structure is calculated as an energy minima.

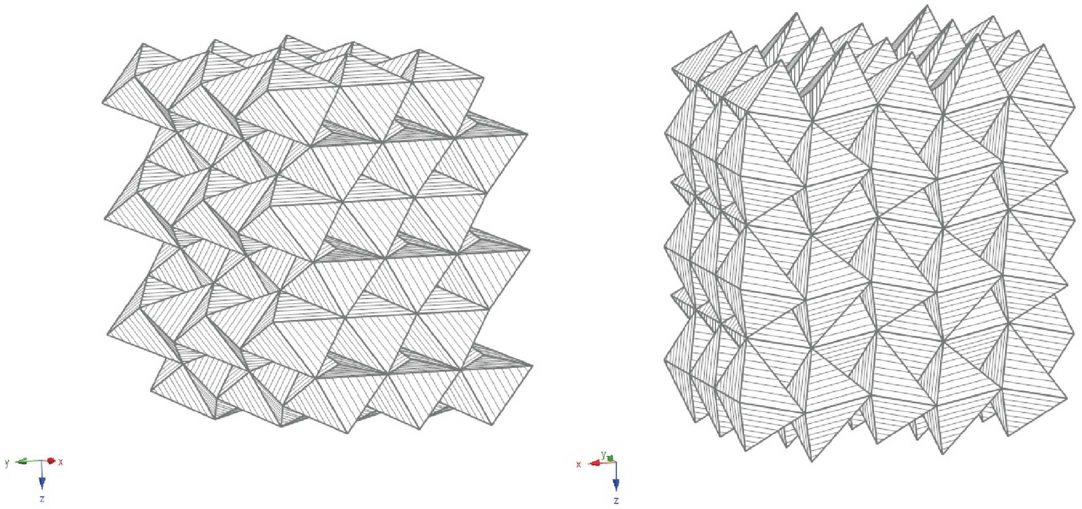

**Figure 3.28:** Experimental (left) and calculated (right) $Li(NH_3)_4BH_4$ structures showing the $LiB_6$ environments. B atoms sit on the corners of the displayed polyhedra.

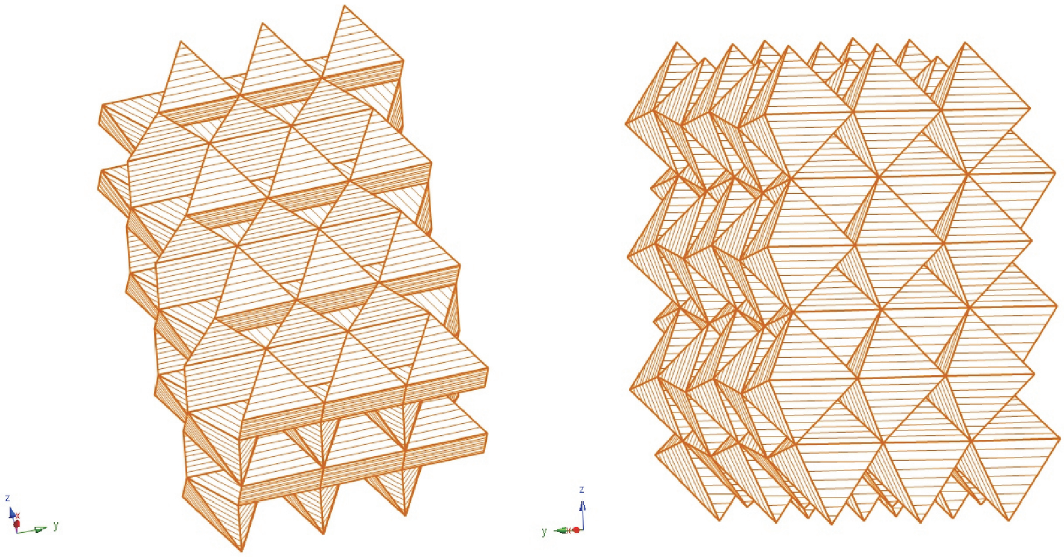

**Figure 3.29:** Experimental (left) and calculated (right) $Li(NH_3)_4BH_4$ structures showing the $BLi_6$ environments. Li atoms sit on the corners of the displayed polyhedra.

## 3.7 Phase Overview and Transitions

All of the presently discussed structures show common features and the evolution from each to the next is clear. Figures 3.30 to 3.33 show that the Li atoms are arranged in pairs that run in rows along either the y-axis or in the case of $Li(NH_3)_3BH_4$ the z-axis. Adjacent rows are organised in layers that run in the yz-plane as Figures 3.34 to 3.37 show. Dihydrogen bonding has been discussed throughout this Chapter and is an important feature in these structures. In each case, adjacent layers appear to be held together by dihydrogen bonding interactions. The different structures are characterised by an increase in both inter- and intra-layer Li−Li distances, with the exception that the inter-layer Li−Li distances are shorter than the intra-layer distances in $Li(NH_3)_3BH_4$.

The enthalpy changes for the reactions of n = 4 to 3, 3 to 2, 2 to 1, and 1 to 0 are calculated from the results of geometry optimisation as 32 $kJmol^{-1}$, 63 $kJmol^{-1}$, 22 $kJmol^{-1}$, and 56 $kJmol^{-1}$ respectively. The phase diagram for these compounds reported by Sullivan and Johnson suggests that these enthalpy changes may only be realistic below about 15 °C, where change between the solid phases occurs. The numbers highlight the similarities and differences between the structures, in particular the low enthalpy change between n = 2 and n = 1 shows the close similarity between these structures while the large enthalpy change between n = 3 and n = 2 highlights the significant change occurring over this transition.

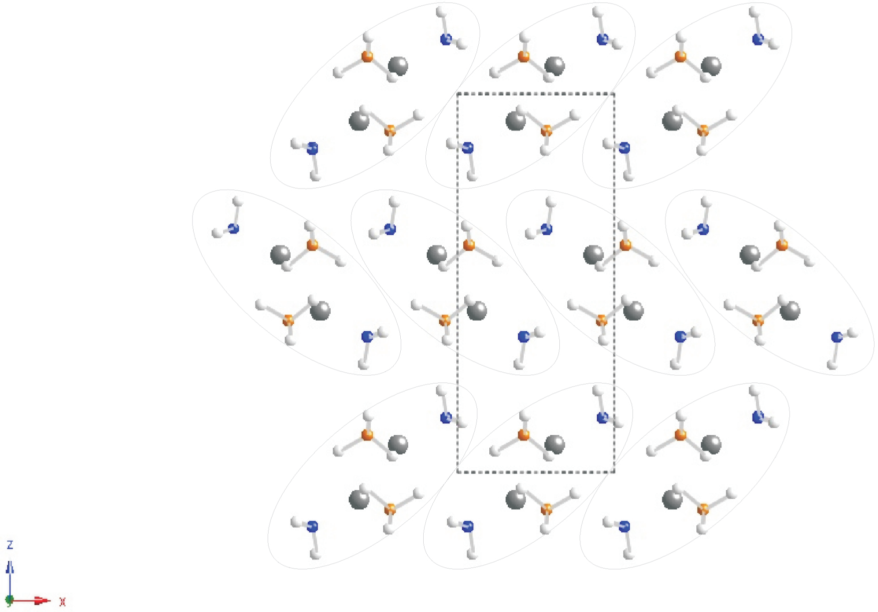

**Figure 3.30:** The Li($NH_3$)$BH_4$ structure, showing the arrangement of rows of atoms running in the y-direction. H atoms are shown in off-white, Li in grey, B in brown and N in blue.

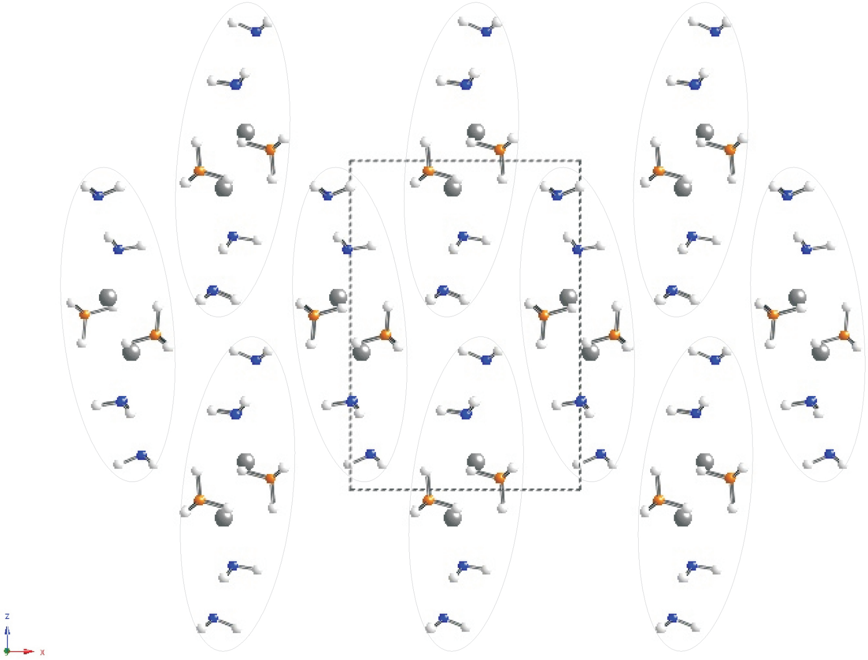

**Figure 3.31:** The Li$(NH_3)_2BH_4$ structure, showing the arrangement of rows of atoms running in the y-direction. H atoms are shown in off-white, Li in grey, B in brown and N in blue.

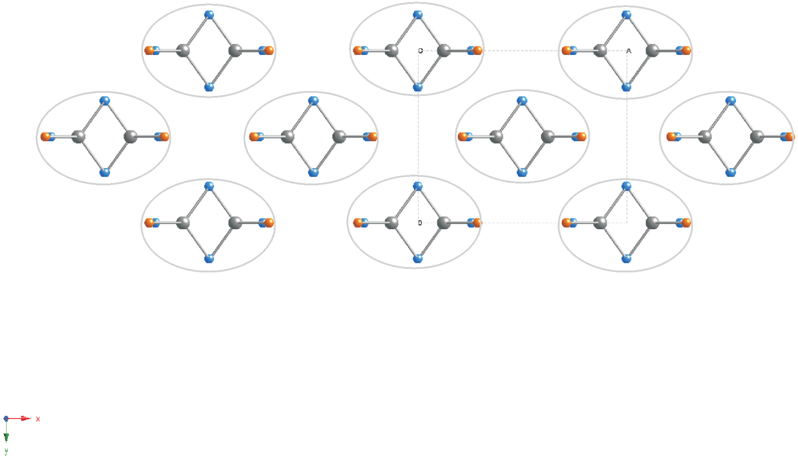

**Figure 3.32:** The $Li(NH_3)_3BH_4$ structure, showing the arrangement of rows of atoms running in the z-direction. H atoms are omitted and Li−N and Li−B bonds are shown for clarity, with Li shown in grey, B in brown and N in blue.

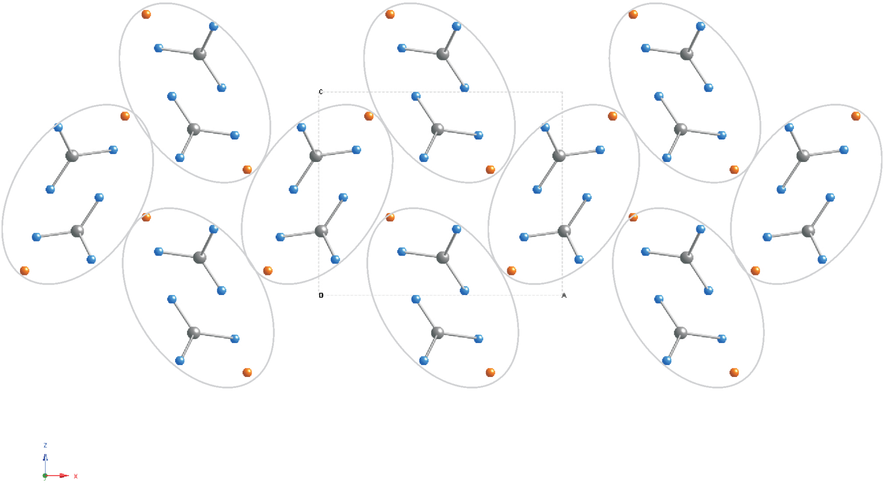

**Figure 3.33:** The $Li(NH_3)_4BH_4$ structure, showing the arrangement of rows of atoms running in the y-direction. H atoms are omitted and Li−N and Li−B bonds are shown for clarity, with Li shown in grey, B in brown and N in blue.

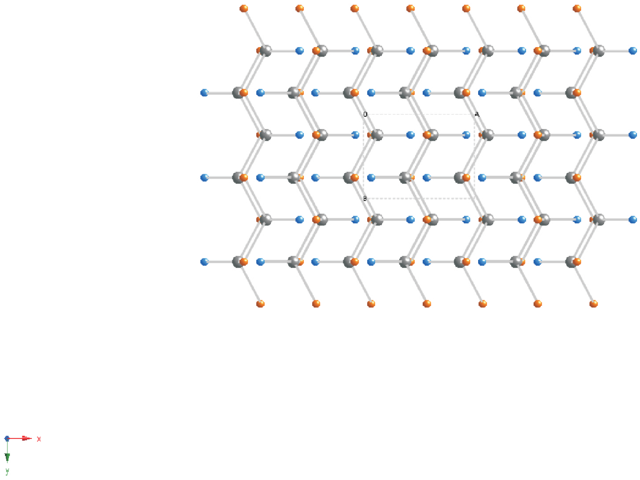

**Figure 3.34:** The Li($NH_3$)$BH_4$ structure, showing the arrangement of layers of atoms running in the yz-plane. H atoms are omitted and Li−N and Li−B bonds are shown for clarity, with Li shown in grey, B in brown and N in blue.

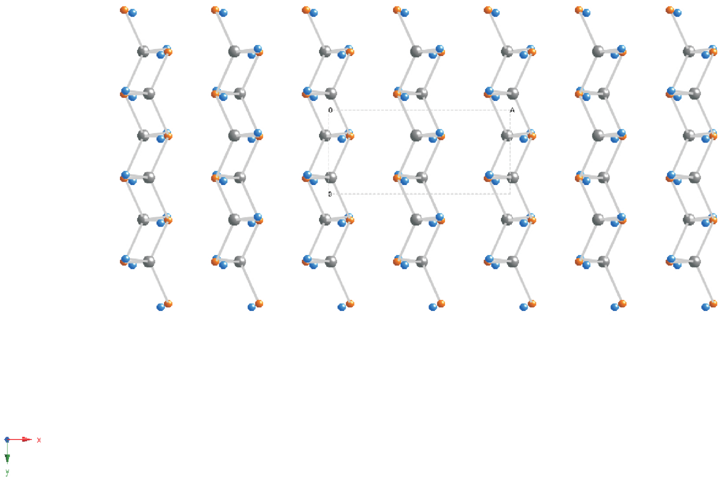

**Figure 3.35:** The Li($NH_3$)$_2$$BH_4$ structure, showing the arrangement of layers of atoms running in the yz-plane. H atoms are omitted and Li−N and Li−B bonds are shown for clarity, with Li shown in grey, B in brown and N in blue.

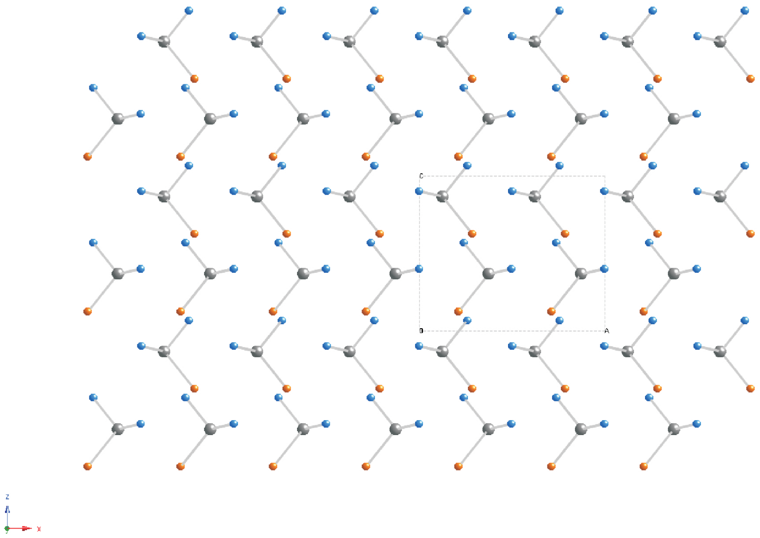

**Figure 3.36:** The $Li(NH_3)_3BH_4$ structure, showing the arrangement of layers of atoms running in the yz-plane. H atoms are omitted and Li−N and Li−B bonds are shown for clarity, with Li shown in grey, B in brown and N in blue.

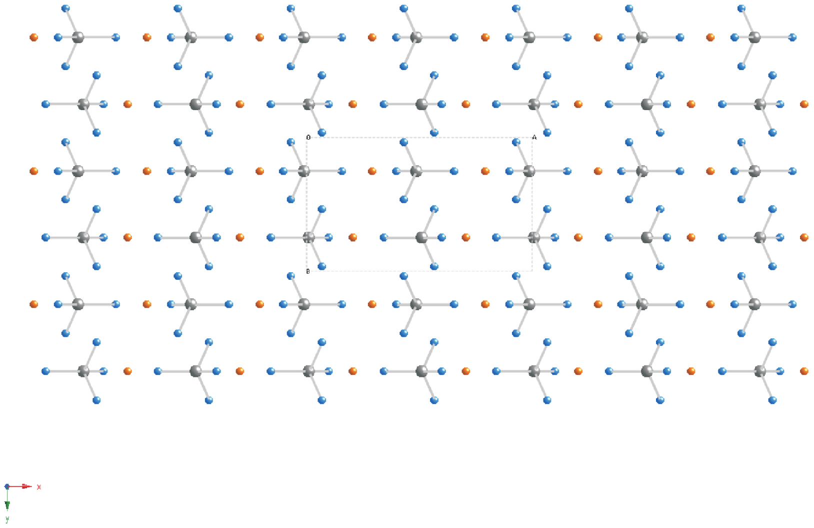

**Figure 3.37:** The $Li(NH_3)_4BH_4$ structure, showing the arrangement of layers of atoms running in the yz-plane. H atoms are omitted and Li−N and Li−B bonds are shown for clarity, with Li shown in grey, B in brown and N in blue.

### 3.7.1 Phase Transitions

During the HRPD IGA$^n$ experiment phase transitions were carried out under isobaric conditions, providing ideal data for studying the kinetics of phase transitions. However the neutron flux on HRPD is low, so in order to gain statistically usable data collection times of 15 minutes were required. Ideally the GEM data would be used for this task given GEM's higher neutron flux, but given the consistent conditions of the HRPD experiment and the improved resolution of the data, the study of these HRPD data is more reliable. In order to study the transition from the n = 4 to the n = 3, 2 and 1 phases, Pawley refinements in the appropriate space groups (given in this Chapter) were carried out across multiple data sets. During refinement all variables were fixed other than the scale factor, which therefore directly represents the proportion of each phase present.

The refined scale factors for the transition between $Li(NH_3)_4BH_4$ and $Li(NH_3)_3BH_4$ are shown in Figure 3.38. As expected it can be seen that the concentration of $Li(NH_3)_4BH_4$ decreases the as the concentration of $Li(NH_3)_3BH_4$ increases. The decrease in $Li(NH_3)_4BH_4$ concentration occurs at a slower rate than the increase in $Li(NH_3)_3BH_4$ concentration, though the reason for this unclear at this stage of investigation.

The transition from $Li(NH_3)_3BH_4$ to $Li(NH_3)_2BH_4$ and $Li(NH_3)BH_4$ is shown in Figure 3.39. It can be seen that (unlike the previous transition) as the intensity of $Li(NH_3)_3BH_4$ reflections decreases, the intensities of the alternative phase reflections do not increase. The non-zero scale factors for $Li(NH_3)_2BH_4$ and $Li(NH_3)BH_4$ below 350 minutes are anomalous and result from the broad peak shape meaning that it is possible to model the data incorrectly using too many trial phases. The fact that these anomalous scale factors decrease along with those for the singularly present $Li(NH_3)_3BH_4$ is indicative of the overall decrease in intensity of all Bragg reflections, which is caused by the formation of liquid $Li(NH_3)_2BH_4$. It should be noted here

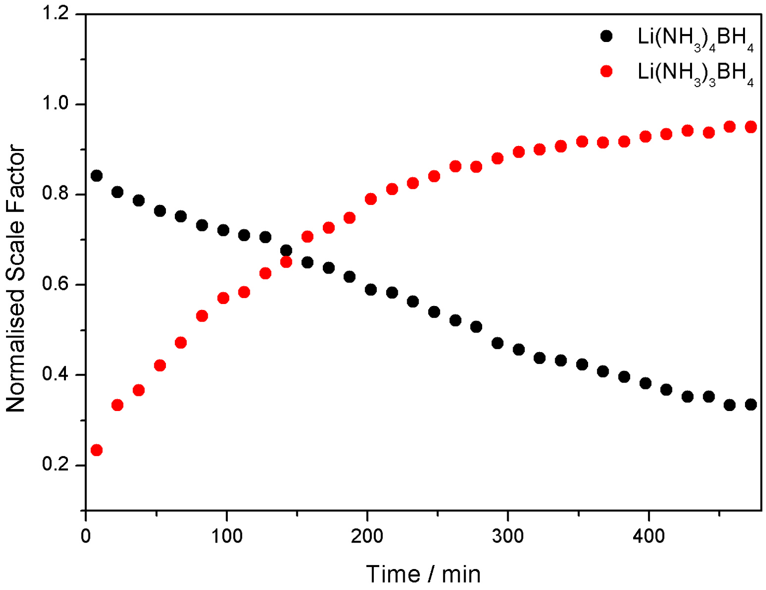

**Figure 3.38:** The normalised scale factors for the transition between $Li(NH_3)_4BH_4$ and $Li(NH_3)_3BH_4$. Data were collected over continuous 15 minute periods using the IGA$^n$ equipment on HRPD and an ammonia pressure of 70 mbar.

that refinements were carried out using all available data and sections of graphs where no datum points are shown, at the expected 15 minute intervals, are a result of the neutron beam cutting out. It can be seen that from a time of 473 minutes $Li(NH_3)BH_4$ begins to crystallise out of the liquid phase, completing the transition from $Li(NH_3)_3BH_4$ to $Li(NH_3)BH_4$ via the liquid $Li(NH_3)_2BH_4$. As may be expected from a crystalline sample grown in-situ, significant preferred orientation is seen in these $Li(NH_3)BH_4$ diffraction data.

The transition from $Li(NH_3)BH_4$ to $LiBH_4$ is demonstrated in Figure 3.40. For these data, due to the neutron beam instability, the plot of scale factors is insufficient to provide any real insight into the reaction. Preferred orientation of both phases also limits the use of inspecting the entire diffraction pattern, however the Figure shows clearly that as the intensity of the $Li(NH_3)BH_4$ reflections drops, the intensity of the $LiBH_4$ reflections increases. It was also observed that in order to model the

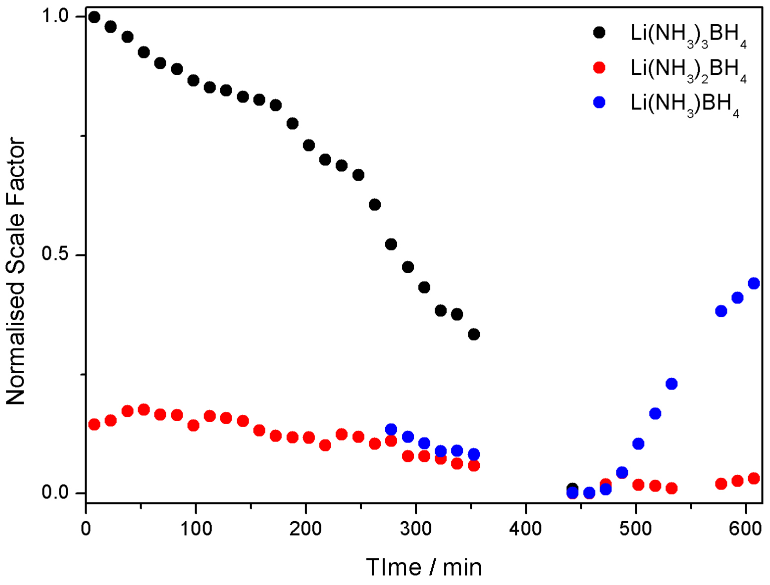

**Figure 3.39:** The normalised scale factors for the transition between $Li(NH_3)_3BH_4$, $Li(NH_3)_2BH_4$ and $Li(NH_3)BH_4$. Data were collected over continuous 15 minute periods using the IGA$^n$ equipment on HRPD, the ammonia pressure was reduced sequentially from 70 mbar to 5 mbar before switching to dynamic vacuum.

$LiBH_4$ phase it was necessary to vary the lattice parameters (a step that was not necessary for modelling any of the other data). This change in lattice parameter is particularly great along the c-axis, as exemplified by the movement of the (002) peak to lower d-spacing that is seen in Figure 3.40. This suggests that as ammonia leaves $Li(NH_3)BH_4$, an intermediate and expanded $LiBH_4$ structure remains and takes some time to relax into the normal $LiBH_4$ phase. This would be an interesting reaction to investigate in greater detail though a greater level of analysis is not possible using the existing data.

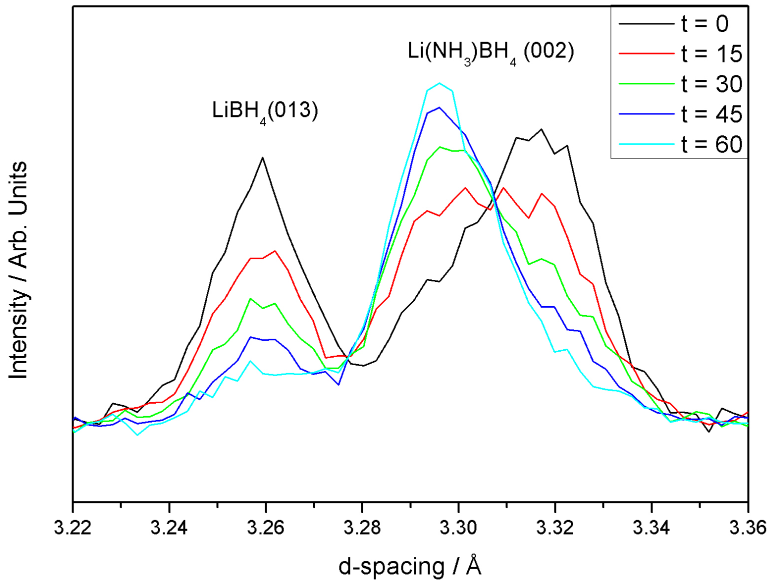

**Figure 3.40:** Diffraction data for the transition between $Li(NH_3)BH_4$ and $LiBH_4$, showing the (013) and (002) reflections for $Li(NH_3)BH_4$ and $LiBH_4$ respectively. Data were collected over continuous 15 minute periods using the $IGA^n$ equipment on HRPD, at a temperature of 50 °C and under dynamic vacuum.

The evidence shown in Figure 3.40 suggests that transition from $Li(NH_3)BH_4$ to $LiBH_4$ occurs completely and there is no trace of other decomposition products. In order to confirm this reversibility a sample of $Li(NH_3)BH_4$ was placed under vacuum in a Schlenk tube and heated to a temperature of 55 °C for a period of 12 hours. The product was a white powder and the diffraction data (shown in Figure 3.41) show only $LiBH_4$ with no trace of either $Li(NH_3)BH_4$ or $LiNH_2BH_3$. This confirms the reversibility of the $Li(NH_3)_nBH_4$ system.

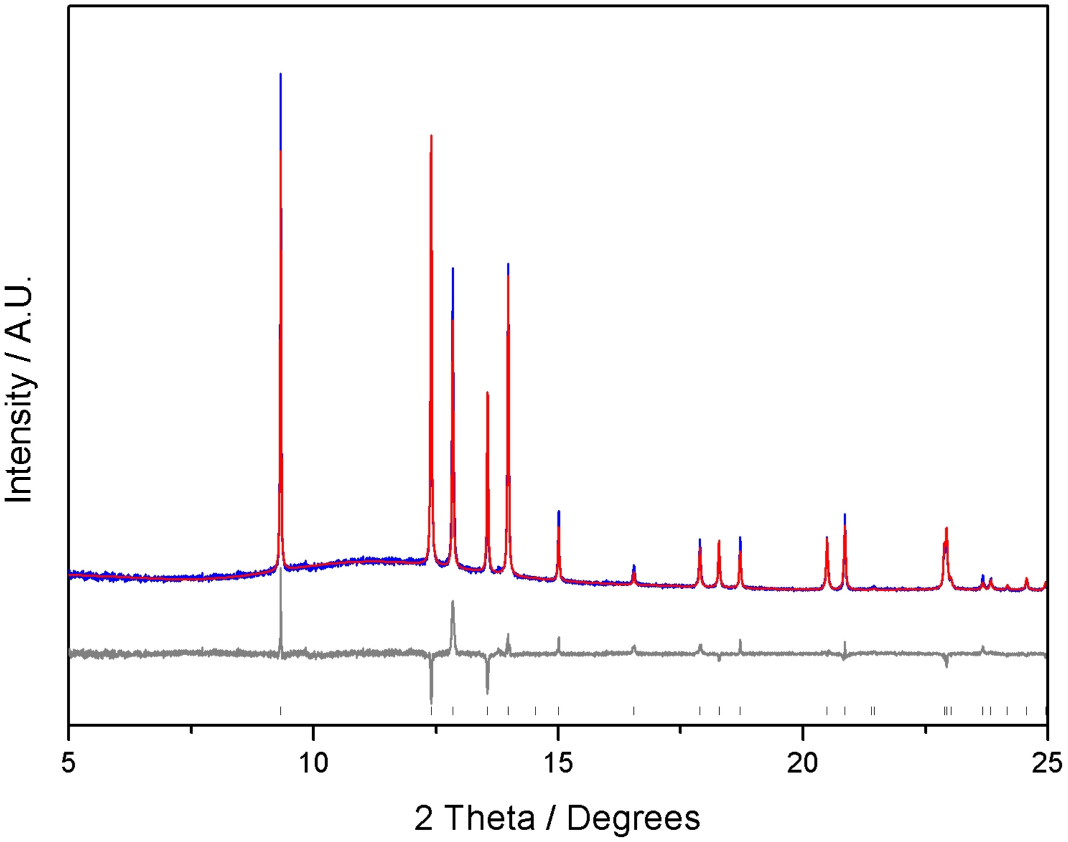

**Figure 3.41:** Final fit to the data for Rietveld refinement of the $LiBH_4$ model to X-ray powder diffraction data from a sample produced by heating $Li(NH_3)BH_4$ to 55 °C under vacuum. Data were collected at the ESRF with a wavelength $\lambda = 0.80268$ Å. Experimental data are shown in blue, calculated in red with the difference in grey, tick marks show the expected positions of Bragg reflections.

### 3.7.2 Low Temperature Phase Transitions

Attempts to isolate $Li(NH_3)_2BH_4$ are briefly discussed in Section 3.4. Two low temperature samples were produced in an attempt to isolate, and collect X-ray diffraction data for, this phase. The first, ‘high temperature,’ sample was prepared by producing a sample of $Li(NH_3)_nBH_4$ in the normal way, and then evacuating the Schlenk tube at 0 °C. The second, ‘low temperature,’ sample was produced in the same way but evacuating at −78 °C. Both samples were transferred to the Diamond Light Source in sealed Schlenk tubes packed in dry ice, and were loaded into capillaries within an argon atmosphere glove bag at temperatures as close to −78 °C as possible. While it was not possible to load the high temperature sample into a capillary tube, data were collected from the low temperature sample. Data collection started at 200 K (−73 °C) and the sample was heated until Bragg reflections disappeared at 358 K (85 °C).

A surface plot of the diffraction data collected between 201 K and 295 K is shown in Figure 3.42, where it can be seen that at least 2 phases exist over this temperature range. Diffraction data (collected at 256 K) for the higher temperature phase are shown in Figure 3.43 where it can be seen that this phase is consistent with $Li(NH_3)_4BH_4$, though in the presence of a $2^{nd}$ unknown phase that is observed in all these diffraction data. In the lower temperature phase it appears that $Li(NH_3)_4BH_4$ has undergone a monoclinic distortion, the transition between the two phases is complete at ca. 231 K upon heating. The phase transition is characterised by the clear splitting of (amongst others) the (111), (011), (112) and (212) peaks, while the (201), (002), (200) and (210) peaks do not split. The new low temperature phase was indexed in the space group $P2_1/n11$, with the lattice parameters of a = 11.6936(6) Å, b = 6.9649(3) Å, c = 10.0324(3) Å and monoclinic angle $\alpha$ = 84.247(6) °C determined by Pawley refinement using Topas. The final fit of the Pawley refined unit cell to the data is shown in Figure 3.44.

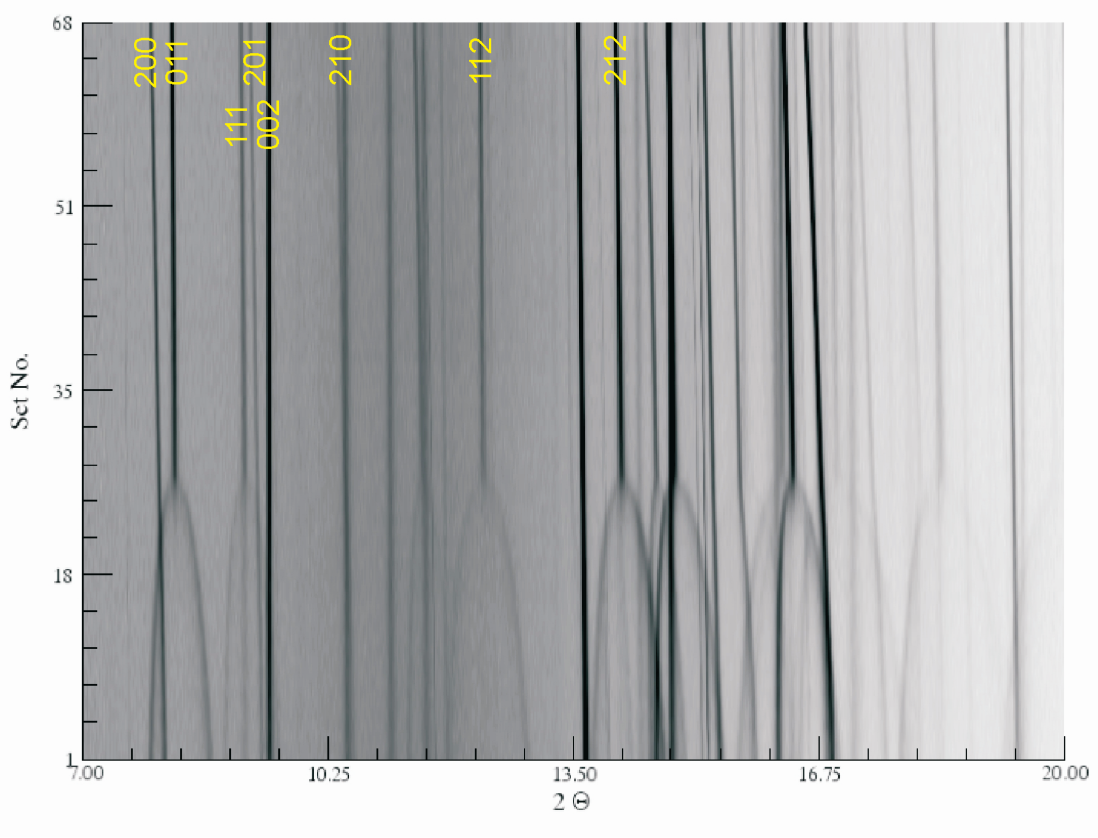

**Figure 3.42:** Surface plot of the diffraction data for the transition between $Li(NH_3)_4BH_4$ low temperature and room temperature phases. Data were collected at Diamond with a wavelength $\lambda = 0.826008$ Å and are plotted with the darkest areas representing the highest intensity peaks. The y-axis represents the run numbers of data that were summed every 10 s when heating between 201 K (top) and 295 K (bottom).

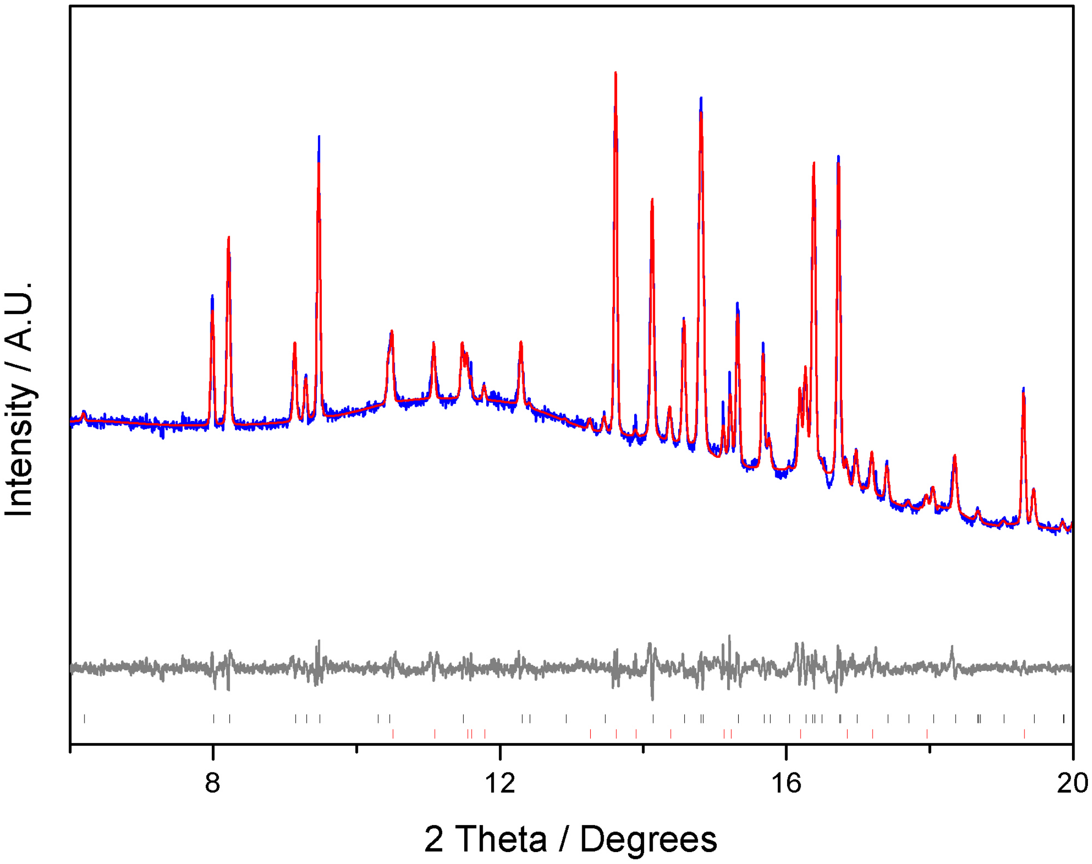

**Figure 3.43:** A Pawley refinement of the $Li(NH_3)_4BH_4$ unit cell to X-ray powder diffraction data collected at the Diamond light source at 256 K and with a wavelength $\lambda = 0.826008$ Å. Experimental data are shown in blue, calculated in red with the difference in grey, tick marks show the expected positions of Bragg reflections for $Li(NH_3)_4BH_4$ in black and an unknown phase in red.

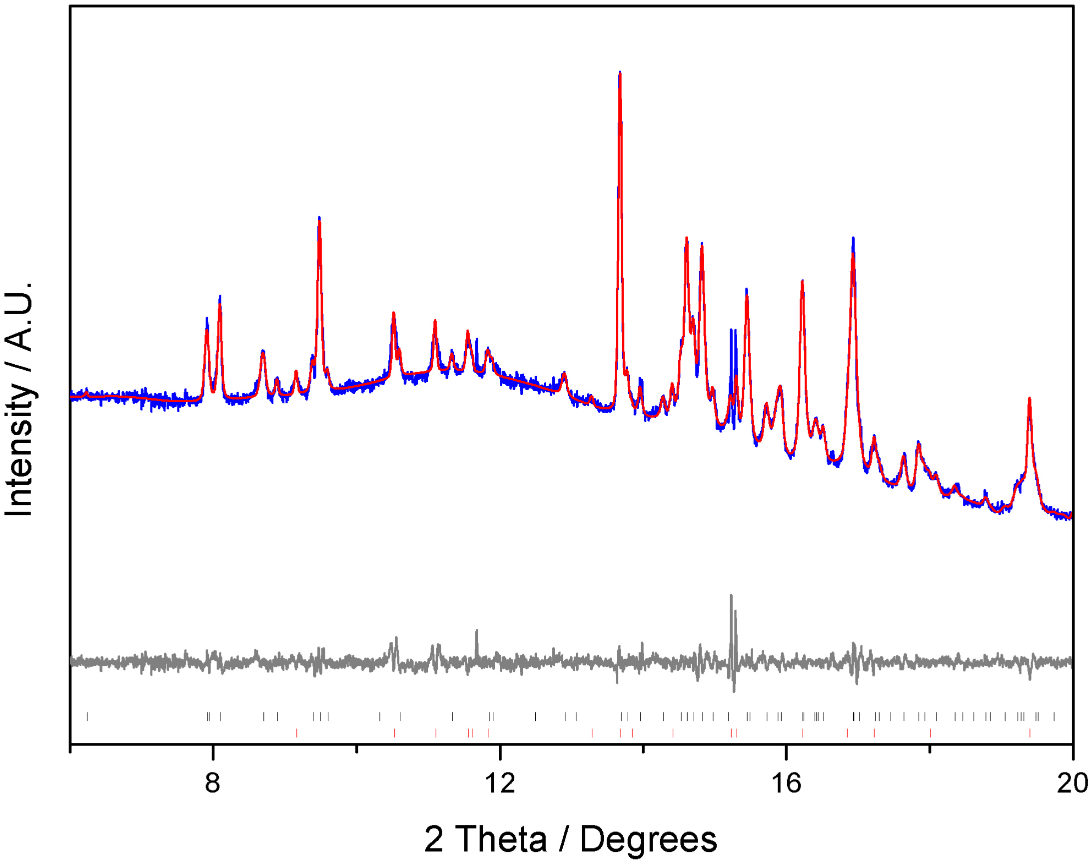

**Figure 3.44:** A Pawley refinement of the LT, monoclinic, phase of Li($NH_3$)$_4$$BH_4$ unit cell to X-ray powder diffraction data collected at the Diamond light source at 201 K and with a wavelength $\lambda = 0.826008$ Å. Experimental data are shown in blue, calculated in red with the difference in grey, tick marks show the expected positions of Bragg reflections for the LT Li($NH_3$)$_4$$BH_4$ phase in black and an unknown phase in red.

## 3.8 Conclusions and Further Work

The structures of $Li(NH_3)_nBH_4$, with n = 4, 3, 2, 1 have been solved using a combination of Rietveld refinement from powder diffraction data and first-principles calculation. Each of the phases has been produced and identified in-situ and thus it has been shown that complete conversion from $LiBH_4$ to $Li(NH_3)_4BH_4$ and back again is possible — $LiBH_4$ acts as a fully reversible ammonia store. Disorder is a common feature of each structure, primarily in the form of multiple ammonia-hydrogen sites but also about the $BH_4^-$ anion in the case of $Li(NH_3)_4BH_4$. A large amount of either dihydrogen or hydrogen bonding is also seen in each case and these bonds act to stabilise the structures.

**$Li(NH_3)BH_4$** is easily synthesised and isolated, dynamic disorder associated with spinning of the ammonia molecule has been observed. Dihydrogen bonding interactions have been shown to be at their greatest within the disordered structure, and explain the weakening of the B−H bond compared to $LiBH_4$. Heating of the sample at a temperature of 50 °C leads to complete conversion to the starting $LiBH_4$.

**$Li(NH_3)_2BH_4$** has been difficult to study due to its low melting point. This low melting point is explained by its open structure and loosely intercalated ammonia. In this compound, NH···HB dihydrogen bonds are reduced in strength compared to $LiBH_4$, and are replaced by NH···N hydrogen bonds which to some extent stabilise the structure but also allow it to melt at low temperatures.

**$Li(NH_3)_3BH_4$** exists at room temperature ammonia pressures of between 30 mbar and 70 mbar, it is stabilised by many weak dihydrogen bonds and adopts a layered structure. It shows low levels of disorder compared to both $Li(NH_3)BH_4$ and $Li(NH_3)_4BH_4$.

**$Li(NH_3)_4BH_4$** exists at room temperature ammonia pressures of greater than 70 mbar and is also stabilised by many weak dihydrogen bonds. High levels of disorder are observed and associated with both the $BH_4^-$ anion and the $NH_3$ molecule. In the case of the $NH_3$ molecule this disorder is likely to be due to a high level of translational ammonia mobility within the structure. It has been shown that this phase orders and undergoes a monoclinic distortion at low temperatures, suggesting that the disorder is dynamic in its nature.

**Further work** in this area would require a detailed study of the reversibility and kinetics of ammonia loading in the system, over tens and hundreds of loading cycles in order to establish the suitability of $LiBH_4$ as a commercially viable ammonia storage material. Further study into the the structure of $Li(NH_3)_2BH_4$ and successful isolation of this phase would also be beneficial. Solving the low-temperature $Li(NH_3)_4BH_4$ structure may well enable a greater understanding of both its structure and the nature of the observed disorder. Another hugely beneficial avenue of research would be to attempt the growth of single crystals of each phase. This may be possible through choosing the correct vapour pressure and slowly evaporating ammonia from a solution of $LiBH_4 \cdot nNH_3$. Subsequent neutron single-crystal diffraction experiments could then be used to both confirm the structures and also gain high quality data with which the nature of the disorder may be unequivocally established.

### 3.8.1 Evaluation as a Storage Material

The results presented here clearly establish $LiBH_4$ as a very promising ammonia storage material. Table 3.11 compares the storage properties of the $Li(NH_3)_nBH_4$ group with liquid ammonia; while these ammines give a reduced ammonia density, significantly they offer greatly reduced vapour pressures. Compared to other ammines with comparable ammonia capacities, for example $Mg(NH_3)_6Cl_2$ or $Ca(NH_3)_8Cl_2$, they have the significant advantage that 75 % of the bonded ammonia molecules may be removed by small changes in the ammonia pressure, with the remaining 25 % of stored ammonia released at the low temperature of ca. 50 °C. Overall these properties mean that storage using $LiBH_4$ may be considered favourable; than liquid ammonia as vapour pressures are reduced and than existing ammines as lower temperatures are required to recover the stored ammonia. Reaction 3.1 shows that that $Li(NH_3)BH_4$ allows storage of 57 wt% ammonia using the room temperature PSA storage method operating between ca. 24 mbar and 110 mbar, this compares preferably to $Ca(NH_3)_8Cl_2$ that can be used to store 41 wt% ammonia using PSA between 700 mbar and 2.1 mbar as shown in Reaction 3.2

$$Li(NH_3)_4BH_4 \longrightarrow Li(NH_3)BH_4 + 3\,NH_3 \tag{3.1}$$

$$Ca(NH_3)_8Cl_2 \longrightarrow Ca(NH_3)_2Cl_2 + 6\,NH_3 \tag{3.2}$$

**Table 3.11:** Summary of ammonia storage properties of $Li(NH_3)_nBH_4$ in comparison with liquid $NH_3$

| Compound | Reversible Ammonia Content / wt% | Ammonia Density / $gL^{-1}$ | Vapour Pressure at 25 °C / mbar | Temperature required for complete ammonia release / °C |
|---|---|---|---|---|
| $Li(NH_3)BH_4$ | 41 | 296 | 6.7 | 50 |
| $Li(NH_3)_2BH_4$ | 61 | 385 | 24 | 50 |
| $Li(NH_3)_3BH_4$ | 70 | 526 | 96 | 50 |
| $Li(NH_3)_4BH_4$ | 76 | 539 | 110 | 50 |
| $NH_{3\,(l)}$ -33°C | 100 | 682 | 1017 | - |

Chapter 4

# Magnesium Halide Ammines

## 4.1 Introduction

Considerable research has been carried out on magnesium halide hexa-ammines, $Mg(NH_3)_6X_2$, but the majority of this has focussed on the chlorides and studies that consider the properties of the group as a whole are uncommon. In this Chapter, the magnesium halides are considered in order to evaluate their ammonia storage properties and to gain an understanding of their chemistry that may be used to interpret the decomposition behaviour of other ammines. Analysis of these ammines has been carried out for the first time using $^{25}$Mg NMR, INS and low-temperature diffraction. Though previous studies have used X-ray diffraction, structural understanding is here developed using unique models and neutron diffraction. The use of DFT has featured heavily in the work of Christensen et. al, and in this work some important properties of the $Mg(NH_3)_nX_2$ system have been calculated and investigated.

## 4.2 Room Temperature Diffraction Studies

All of the $Mg(NH_3)_6X_2$ group are expected to share the same $K_2PtCl_6$ structure, and as discussed in Section 1.4.2 the $Fm\bar{3}m$ space group does not allow for a molecule with 3-fold rotational symmetry, thus the hydrogen atoms of the $NH_3$ molecules must be disordered. The disorder within the structure means that it can be challenging to model diffraction data, but successful modelling may lead to greater understanding of the structure and material properties. In order to gain a greater understanding of these structural intricacies, both neutron and X-ray diffraction experiments were carried out at room temperature and at variable temperatures from 10 K to 150 K.

### 4.2.1 X-Ray Powder Diffraction

Room temperature X-ray powder diffraction studies of $Mg(NH_3)_6X_2$ (X = Cl, Br, I) were carried out using beam line I11 at the Diamond Light Source. The cubic ($Fm\bar{3}m$) $K_2PtCl_6$ structure was used to model the data using Rietveld refinement. The cubic lattice parameter, a, was allowed to vary freely while the positions of the Mg and X atoms were fixed on the appropriate special positions within the unit cell. The positions of the N and H atoms were allowed to vary freely along the y-direction. The N−H bond length was constrained between values of 0.9 Å and 1.1 Å, and the MgNH bond angle between 105 ° and 115 °.

To model the disorder in its most general form, the scattering from the hydrogen atoms of the $NH_3$ molecules is best delocalised around a ring of radius and position determined by the N−H bond length and MgNH bond angle; the overall occupancy of this ring should give an H:N ratio of 3:1.[i] In practice it was simpler to model the hydrogen atoms positioned at 15 ° intervals around the ring, giving each of the 24 hydrogen sites an an occupancy of 3/24, an image of this model is shown in Figure 4.1. In principle with neutron or single-crystal diffraction data it would

---

[i] This approach is exemplified in analysis of the single crystal data discussed in Section 3.3.3

be possible to determine the favoured hydrogen sites about the ring. From powder X-ray diffraction alone it is not possible to unambiguously determine the hydrogen atom positions on this circular locus. However, for the purposes of comparison within a series of isostructural materials this approach provides the most accurate and appropriately constrained model for structural solution. Figure 4.2 shows a typical fit of the model to diffraction data, in this case the $Mg(NH_3)_6Br_2$ data are shown with the remaining diffraction data displayed in Appendix E.4 and E.5.

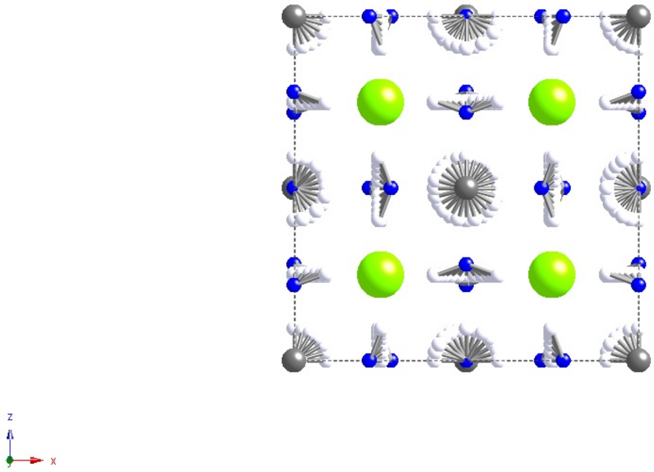

**Figure 4.1:** The disordered $Mg(NH_3)_6Cl_2$ model used for analysis of diffraction data showing hydrogen sites positioned every 15 ° about a circular locus. Magnesium is shown in grey, nitrogen in blue, hydrogen in off-white and chlorine in lime green.

The refinements confirm that each of the ammines shares the cubic $K_2PtCl_6$ structure, as reported for $Mg(NH_3)_6Cl_2$, and suggested for $Mg(NH_3)_6Br_2$ and $Mg(NH_3)_6I_2$.[30,31,33,34] A comparison of the refined unit cell sizes and bond lengths is given in Table 4.1. It can be seen that the Mg−N distance increases slightly as the size of the anion increases. This suggests that the strength of the Mg−N bonding decreases with increasing size of the anion. This can be explained by the smaller more electronegative anions causing a reduced electron density on the entire $Mg(NH_3)_6^{2+}$ cation. Given its lower electronegativity, this positive charge will

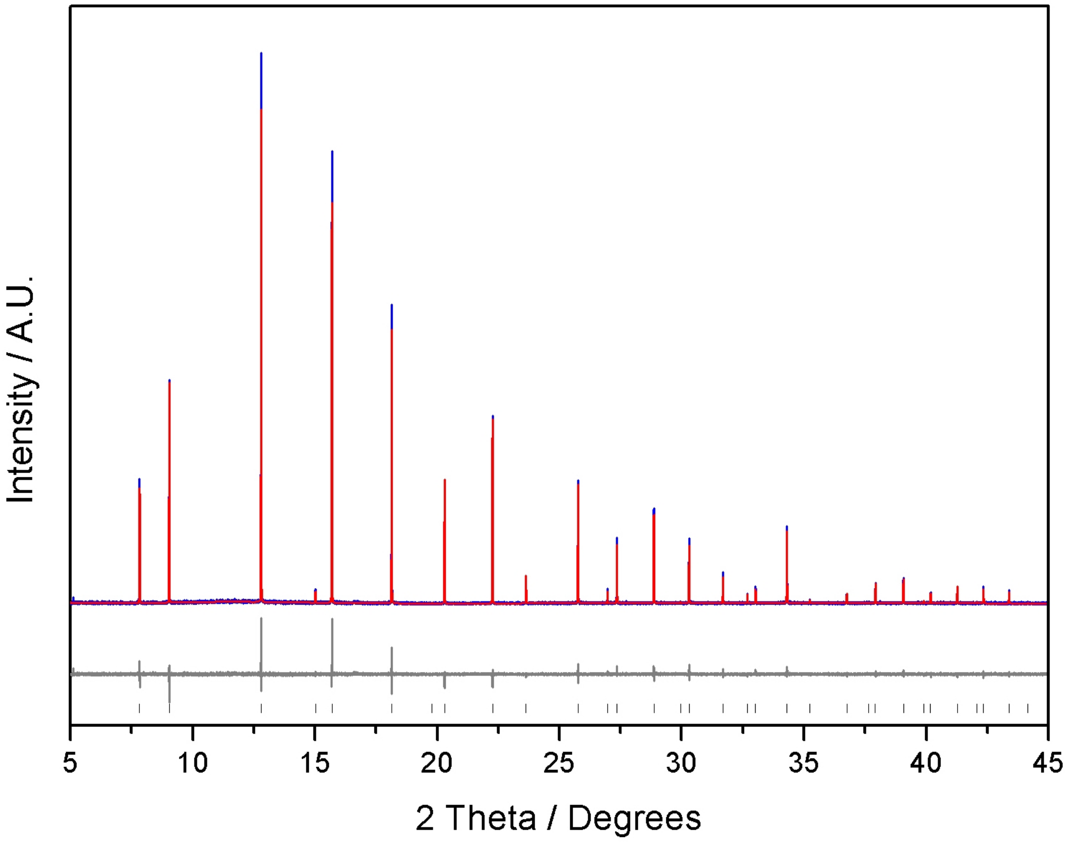

**Figure 4.2:** The final fit to the data for Rietveld refinement of the $Mg(NH_3)_6Cl_2$ model to X-ray powder diffraction data collected at the Diamond Light Source using a wavelength $\lambda = 0.82000$ Å. Experimental data are shown in blue, calculated in red with the difference in grey, tick marks show the expected positions of Bragg reflections.

remain principally on the Mg nucleus, resulting in stronger Mg−N bonding, though the effect is small in magnitude. The Mg−N bond lengths are similar in magnitude to those observed in the crystal structures of $Mg(NH_3)_2X_2$ for which Leineweber reports 2.125(3) Å for X = Cl and 2.108(3) Å for X = Br. The implication from these two bond lengths is that the bond strength trend is reversed in the di-ammine. However, the data for the bromide were collected at a temperature of 25 K, lower than those for the chloride and this may well account for the reduced bond length. Further investigation would be required to comment on this trend and its significance. There was no significant change in the N−H bond length or MgNH angle although this may be due to limitations of the X-ray powder diffraction data. The final refined atomic positions are given in Appendix E.2, E.3 and E.4.

**Table 4.1:** Unit cell parameters and Mg−N bond lengths in $Mg(NH_3)_6X_2$, refined from X-ray powder diffraction data.

|  | $Mg(NH_3)_6Cl_2$ | $Mg(NH_3)_6Br_2$ | $Mg(NH_3)_6I_2$ |
|---|---|---|---|
| a / Å | 10.12258(3) | 10.40693(1) | 10.91487(2) |
| Mg−N Length / Å | 2.161(2) | 2.167(3) | 2.181(4) |

### 4.2.2 Neutron Powder Diffraction

Neutron powder diffraction data for $Mg(ND_3)_6Cl_2$ were collected using GEM at ISIS. Data were collected by the research group of P. J. van Ekeren but as no publications arose from their measurements and the group later disbanded, these data were released by ISIS for analysis in this Thesis. Data were collected at various temperatures and pressures, and analysis was preceded by subtraction of the complicated background pattern from all data. In-depth analysis of the experiment is hard given that the conditions are vague and on inspection of the data with the best count statistics it was observed that most of the data are of poor quality. A single set of data collected under 1.5 bar $ND_3$ at 120 °C (393 K) produces a reasonable pattern.

Extrapolating from the TGA data discussed in Section 4.5, $Mg(ND_3)_6Cl_2$ should be the predominant phase under these conditions. Using the same model that was refined against the X-ray diffraction data, and refining against data collected using GEM banks 3, 4 and 5 (34 °, 62 ° and 92 ° respectively) a good fit to the data, with $\chi = 1.699$, was achieved. The quality of the fit was similar for each bank, exemplified by that for bank 3 as shown in Figure 4.3. In principle, neutron data should allow the positions of greatest deuterium density about the locus to be determined. Allowing the the occupancies of the four deuterium sites to vary gave values of 0.009, 0.003, 0.084 and 0.490 for the 0 °, 15 °, 30 ° and 45 ° sites respectively. These occupancies may not be quantitatively correct, but a clear preference for the 45 ° site is shown. Referring to Figure 4.1, the 0 ° site is in line with any of the axes, and the 45 ° site aligns the N−D bond with a $Cl^-$ anion. The refined $ND \cdots Cl^-$ distance is 2.660 Å, which is similar to the ClH···ClH distance of 2.589 Å seen in solid HCl.[104] The implication of this is that there is slightly weakened hydrogen bonding between N−D and $X^-$. This result agrees with the observations of Lienweber et. al. and Hoser et. al. who report hydrogen bond driven site preference in the disordered structures of $Mg(ND_3)_2Cl_2$ and $Ni(ND_3)_6Br_2$ respectively.[39,45]

Diffraction data for $Mg(ND_3)_6Cl_2$ were also collected using HRPD at a temperature of 95 K during the low-temperature experiment discussed in Section 4.3. The high flux of GEM should make it the superior instrument for studying this kind of disorder, but the HRPD data has the advantage of not being subject to any post collection manipulation (the improved resolution of HRPD does not help in this case as the highly symmetrical cubic structure produces few Bragg reflections that are close to their neighbours). Using the same model as for the GEM data and refining against data collected using banks 1 and 2 (168 ° and 90 ° respectively) a good fit to the data, with $\chi = 2.137$, was obtained. Repeating the same process and allowing the occupancies of the four deuterium sites to vary gave values of 0.014, 0.001, 0.083 and 0.500 for the 0 °, 15 °, 30 ° and 45 ° sites respectively. Once again a strong

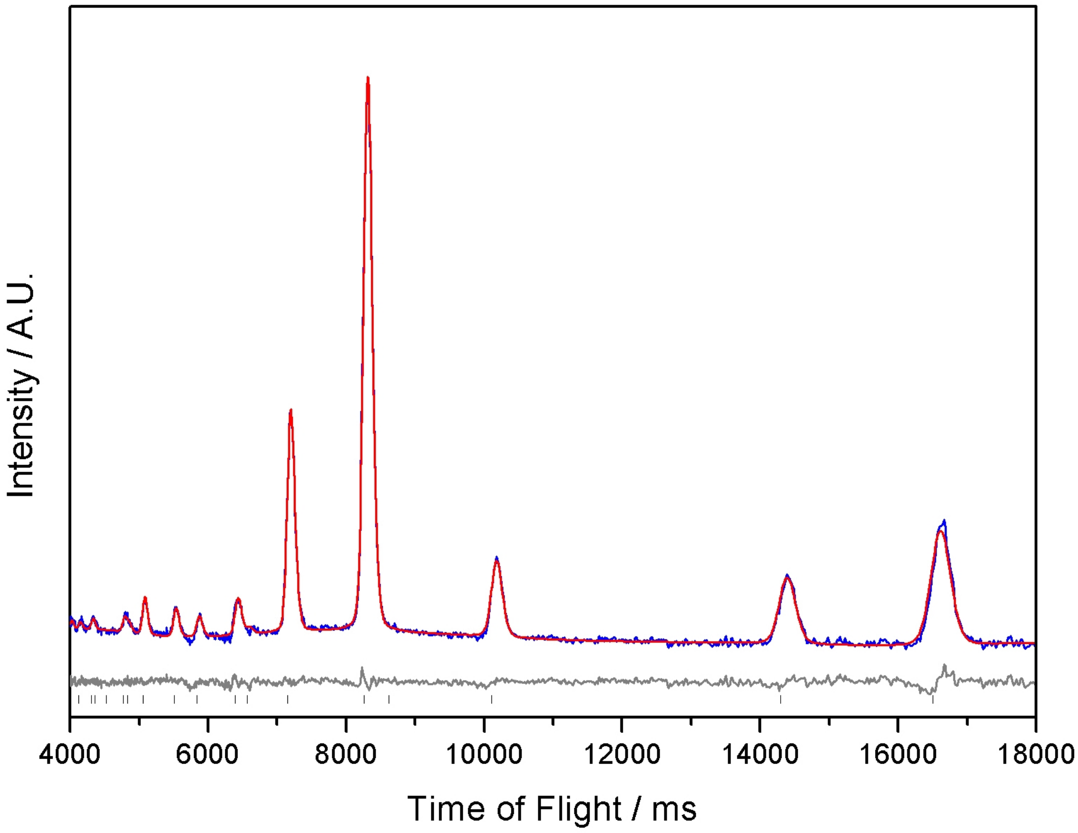

**Figure 4.3:** Final fit to the data for Rietveld refinement of the $Mg(NH_3)_6Cl_2$ model to neutron powder diffraction data, collected using GEM bank 3 (34 °) by van Ekeren et. al.. Experimental data are shown in blue, calculated in red with the difference in grey, tick marks show the expected positions of Bragg reflections.

preference for the 45 ° is observed. Compared to the GEM refinement, a shorter ND···Cl distance of 2.634 Å reflects a global reduction in unit cell parameters, which is expected for a lower temperatures. A comparison of some useful data from the GEM and HRPD refinements is given in Table 4.2.

**Table 4.2:** A comparison of selected $Mg(ND_3)_6X_2$ data, refined from neutron powder diffraction data collected using GEM and HRPD.

| | GEM | HRPD |
|---|---|---|
| T / K | 393 | 95 |
| a / Å | 10.2450(11) | 10.0899(17) |
| Mg−N Length / Å | 2.272(4) | 2.210(3) |
| N−D Length / Å | 0.995(56) | 0.995(26) |

## 4.3 Low Temperature Diffraction Studies

Given the disorder at room temperature, it is highly likely that $Mg(NH_3)_6Cl_2$ adopts an ordered structure at low temperatures. Initial experiments were carried out at the ESRF to investigate any low temperature phases, these experiments were then extended using HRPD at ISIS.

### 4.3.1 X-ray Powder Diffraction

Initial analysis shows that two phases exist; the $Fm\bar{3}m$ high temperature (HT) phase, and a second low temperature (LT) phase, though the HT phase was observed in all collected data. Initial inspection of the ESRF data revealed transitions occurring at different temperatures, with the high temperature phase dominant at temperatures as low as 12 K, and the low temperature phase dominant up to temperatures of 66 K. To some degree this disparity in transition temperatures may be due to hysteresis, however on cooling from 54 K to 10 K negative thermal expansion, that was not seen in other parts of the experiment, was observed. Furthermore, and